Hot primary melts and mantle source for the Paraná-Etendeka flood basalt province: New constraints from Al-in-olivine thermometry

Eleanor S Jennings[a,b]*, Sally A Gibson[a], John Maclennan[a]

[a]Department of Earth Sciences, University of Cambridge, Downing Street, Cambridge, CB2 3EQ, United Kingdom

[b]Department of Earth and Planetary Sciences, Birkbeck, University of London, Malet Street, London, WC1E 7HX, United Kingdom *corresponding author: e.jennings@bbk.ac.uk

Keywords: olivine; thermometry; Al-in-olivine; continental flood basalt; Paraná-Etendeka; mantle plume; mantle temperature

Authors' accepted manuscript. Accepted 26/08/2019 for publication by Chemical Geology; see published version at https://doi.org/10.1016/j.chemgeo.2019.119287

Abstract

Continental flood basalts (CFB) are amongst the most voluminous volcanic eruptions in Earth's history. They are rapidly emplaced, and in rare cases the thick lava piles are associated with primitive magmas that have high MgO contents. The compositions of these primitive melts are consistent with a deep-sourced, high-temperature mantle plume origin. Whilst the association of CFBs with impacting mantle plumes is widely accepted, the magnitude of the thermal anomaly is not yet resolved. The development of Al-in-olivine thermometry, however, allows the crystallisation temperature of (near-)liquidus olivine to be determined without using the composition of the co-existing melt. This provides both a robust minimum estimate of mantle temperature and a value from which potential temperature (T_P) can be back-calculated. This technique has previously confirmed that crystallisation temperatures in CFB settings can be a few hundred degrees greater than those estimated for MORB, and the results hint at a diversity in crystallisation temperatures between different CFB settings.

In this study, we re-assess the T_P of the mantle source of the Paraná-Etendeka CFB province by applying the Al-in-olivine thermometer to olivine-spinel pairs from picrites and ferropicrites. We show that the mean crystallisation temperatures of olivine with $Fo_{>90}$ in the picrites is 1458 °C, with a maximum temperature of 1511 °C. Using the mean value, we calculate a preferred T_P of 1623 °C, for an assumed lithospheric thickness of 50 km and magma emplacement pressure of 0.5 GPa. This represents a thermal anomaly of around +300 °C relative to ambient mantle, and confirms that the mantle source of the Paraná-Etendeka CFB is the second hottest known from Phanerozoic Large Igneous Provinces, after the Caribbean Large Igneous Province. The ferropicrites record a cooler mean olivine crystallisation temperature of 1296 °C. Given that these low-volume melts derive from deeper and earlier melting of mantle pyroxenite, their temperature is not directly comparable to that of the picrites but they appear to require a somewhat cooler mantle source – perhaps found at the front or edges of a rising plume head.

1 Introduction

1.1 Petrological estimates of mantle temperature

The enormous volumes of magma that formed continental flood basalt (CFB) provinces, and their rapid eruption rates, represent significantly higher magmatic fluxes than the eruptions occurring on Earth's surface today (e.g. Renne et al, 2015). These vast outpourings of CFB lavas are widely considered to be responsible for global environmental change and extinction events throughout the geological record (e.g. Saunders, 2016; Sobolev et al., 2011; Song et al., 2013; Wignall, 2001). The theory that the starting heads of upwelling thermal plumes in the mantle are responsible for CFB provinces is now widely accepted (e.g. Herzberg et al., 2007; Morgan, 1971; Putirka et al., 2007; Richards et al., 1989; White & McKenzie 1989, 1995). The temperatures of the starting plume heads are less well constrained. This uncertainty is important because thermal convection is a key mechanism by which planets lose their internal heat: understanding the occurrence and properties of upwelling plumes, including their thermal history, has implications for interpreting the spatiotemporal patterns of volcanism both on our planet and others.

Temperature variations in the convecting mantle are conveniently described by the concept of *potential* temperature, T_P, which is its temperature extrapolated along a solid adiabat to 1 bar (McKenzie and Bickle, 1988). If mid-ocean ridges remote from hotspots sample the ambient mantle (Parsons and Sclater, 1977), then a thermal anomaly in the mantle has an elevated T_P relative to that of the MORB-source mantle. The T_P of the mantle can be investigated through its melts, with the most primitive magmas retaining properties that are easiest to relate to the mantle source. Techniques involving FeO-MgO olivine-melt equilibrium have been used to obtain crystallisation temperatures of the most primitive melts, which can be considered minimum estimates of T_P (Beattie, 1993; Roeder and Emslie, 1970). However, these techniques require a well-constrained estimate of the equilibrium melt composition, and will be inaccurate if olivine

compositions have undergone re-equilibration during slow cooling. Alternatively, parameterisations of mantle melting experiments have been used to relate the compositions of magmas to peridotite melting at different T_P conditions (Herzberg and Asimow, 2015; Langmuir et al., 1992; McKenzie and Bickle, 1988).

The development of the Al-in-olivine thermometer (Wan et al., 2008) and its refined calibration (Coogan et al., 2014) have provided an alternative method to investigate T_P that is: (i) independent of melt composition; and (ii) more robust to post-crystallisation processes, such as chemical changes in the magma from fractionation and assimilation, and diffusive re-equilibration of the olivine. The Al-in-olivine thermometer records the equilibrium temperature of olivine–spinel pairs, which is effectively the temperature at which these two phases co-saturate at, or near, the liquidus of primitive melts. Al-in-olivine thermometry has been successfully applied to several CFB provinces, Iceland, and MORB (Coogan et al., 2014; Heinonen et al., 2015; Matthews et al., 2016; Spice et al., 2016; Trela et al., 2017; Xu and Liu, 2016). The equilibration temperature variations of several hundred degrees are consistent with significant thermal anomalies in the mantle. Whilst this technique has shown that crystallisation temperatures in CFB settings can be much greater than those in MORB, it has also highlighted a diversity in crystallisation temperatures, and perhaps T_P, between different CFB settings.

1.2 The Paraná-Etendeka Continental Flood Basalt Province

The Early Cretaceous Paraná-Etendeka Large Igneous Province (LIP) outcrops in South America and south west Africa (Erlank et al., 1984; Peate, 1997; Thompson et al., 2001). Unusually, the main pulse of CFB volcanism is not associated with a major extinction event or climatic change, despite its large size and high emplacement rate (Wignall, 2001). A recent study has shown that some samples of primitive olivine-rich melts in the Paraná-Etendeka CFB province have high $^3He/^4He$ (> 26 R/R_A), which was interpreted as evidence of a deep mantle plume source (Stroncik et al., 2017). The Paraná-Etendeka CFB province is also convincingly

related to the modern-day Tristan mantle plume through two complementary seamount ridges across the Atlantic seafloor (e.g. White and McKenzie, 1989).

As with most CFB provinces, the main-sequence of flood lavas are not particularly useful for understanding mantle melting conditions, as they have been extensively altered by fractionation and assimilation processes (e.g. Arndt et al., 1993; Erlank et al., 1984; Peate, 1997). Fortunately, outcrops of more primitive rock types — picrites and ferropicrites — are exposed in the Namibian portion of the Paraná-Etendeka CFB province: these are found predominantly as dykes that are part of the plumbing system of the overlying flood lavas and associated volcanics (Erlank et al., 1984; Marsh et al., 2001; Thompson et al., 2001). These magmas bypassed the fractionation and assimilation processes responsible for the chemical processing of the flood basalts, and retain properties imparted by mantle melting. The ferropicrites represent the earliest magmatic products in this province, as well as in many others (Gibson et al., 2000; Gibson, 2002). The more common picrites are thought to derive from high-fraction melting in the central stem of the Tristan plume, and thus are genetically related to the flood basalts, providing a window into the physical and chemical properties of their mantle source (Jennings et al., 2017; Thompson et al., 2001; Thompson and Gibson, 2000).

Previous estimates of the T_P of the Paraná-Etendeka plume source derived from the picrites are contradictory, but indicate a mantle source temperature well above that of ambient mantle (Thompson and Gibson, 2001; Keiding et al., 2011). A significant limitation of the previously-available techniques was that they required the melt composition to be known, and so different methods of calculating the primary melt composition have resulted in different T_P estimates. Thompson and Gibson (2000) used the maximum olivine forsterite (Fo) content and whole-rock MgO–Fe/Mg relationships to infer a komatiitic primary melt composition, implying an extremely high corresponding T_P of ~1680 °C. By contrast, Keiding et al. (2011) used melt inclusion compositions from high-Fo olivine to define a primary melt that is much lower in MgO and corresponds to a lower T_P of ~1520 °C. These two approaches and results are further

discussed in section 4.2.1. In this study, we use the Al-in-olivine thermometer, which is independent of melt composition, to investigate crystallisation temperatures of primitive melts and calculate the T_P of the mantle source of the Paraná-Etendeka CFB province, in order to understand the magnitude of the mantle thermal anomaly that was responsible for the creation of this voluminous CFB province.

2 Materials and methods

2.1 Samples

The samples used in this study are Early Cretaceous (132–133 Ma) picrites and ferropicrites from the Etendeka region of NW Namibia, part of the Paraná-Etendeka CFB province. They are the same set as those used by Jennings et al. (2017) and were previously described by Thompson et al. (2001), Thompson and Gibson (2000) and Gibson et al. (2000); detailed descriptions can be found in those studies. Sample localities are shown in Supplementary Figure S1.

The picrites are from dykes near Horingbaai (known in the literature as "Horingbaai-type" of the high-Ti suite; Marsh et al., 2001). They contain 0.5–2 mm olivine macrocrysts with cores of up to Fo_{93}, and appear to represent near-primary melts rather than having a cumulate origin (Thompson et al., 2001). The Horingbaai picrites have previously been suggested to derive from high-temperature, high-fraction melting of peridotite in the sub-lithospheric mantle, followed by the crystallisation of phenocrysts (Jennings et al., 2017; Thompson et al., 2001; Thompson and Gibson, 2000). The olivine compositions range from a maximum Fo_{93} and 4400 ppm Ni in cores of macrocrysts from some samples to a minimum of Fo_{70} and 1000 ppm Ni in rims and small crystals. High-forsterite crystals sometimes contain Cr-spinel inclusions. Olivine ± plagioclase macrocrysts are set within a fine-grained groundmass. The morphologies of olivine in the picrites vary between and within samples: some contain equant olivine macrocrysts; others have olivines with morphologies indicative of more rapid growth (e.g. hopper, skeletal and tubular crystals, and high aspect ratios). Three picrite samples with high-Fo olivines of different morphologies

were analysed by QEMSCAN at the University of Cambridge, which performs phase identification on a pixel-by-pixel basis from EDS measurements of composition (see Supplementary Figure S2 for images; see Neave et al., 2017, for technical details). The scans showed no obvious correlation between Fo content and olivine morphology, and the presence of delicate, highly-elongate crystals consisting of $Fo_{>90}$ in some samples is evidence for the in-situ growth of these crystals from a high-MgO melt. The olivine and whole-rock samples are generally not far from equilibrium ($K_{D_{\text{Fe-Mg}}}^{\text{ol-WR}} \sim 0.30$), indicating that the high MgO content of the whole-rock samples is not usually caused by olivine accumulation. The sample with the most forsteritic olivine, 97SB33, contains 13.6 wt.% MgO. A QEMSCAN of this particular sample indicates an olivine mode of 13.5% with no other phenocrysts, allowing the liquid composition to be reconstructed from whole-rock data: the resultant $K_{D_{\text{Fe-Mg}}}^{\text{ol-liq}} = 0.14$ indicates that this rock has in fact lost a large fraction olivine macrocrysts, indicating that the melt from which the olivine crystallised had a significantly higher MgO content.

The Paraná-Etendeka ferropicrites are olivine-phyric (up to Fo_{86}) and may also contain macrocrysts of sub-calcic augite set in a fine-grained groundmass that is rich in opaque oxides. The ferropicrites have olivines with low Fo but similarly high Ni contents to those in the picrites. On the basis of their Fe-rich and Al-poor major element composition, anomalously low HREE abundances, and other features of their elemental and isotopic compositions the ferropicrites have been interpreted as resulting from the melting of mantle pyroxenite at high pressures and temperatures (Gibson, 2002; Jennings et al., 2016; Tuff et al., 2005).

2.2 Al-in-olivine thermometry

The Al-in-olivine thermometer exploits the fact that aluminium becomes less incompatible in olivine with increasing temperature (e.g. Wan et al., 2008; De Hoog et al., 2010). This thermometer uses the partition coefficient of Al between spinel and olivine ($k_d = Al_2O_3^{\text{olivine}} / Al_2O_3^{\text{spinel}}$, in wt. %) and has been experimentally calibrated for a range of temperatures and a

limited range of mafic-ultramafic compositions by Wan et al. (2008) and Coogan et al. (2014).

$$T(\mathrm{K}) = \frac{10000}{0.575(0.162) + 0.884(0.043)\mathrm{Cr\#} - 0.897(0.025)\ln k_{\mathrm{d}}} \quad [1]$$

where $\mathrm{Cr\#} = X_{\mathrm{Cr}}^{\mathrm{spinel}} / (X_{\mathrm{Cr}}^{\mathrm{spinel}} + X_{\mathrm{Al}}^{\mathrm{spinel}})$, in atomic %, and the values in parentheses are the published standard error of the parameter

When olivine and spinel simultaneously saturate and grow in the same melt, we assume they are in equilibrium with one-another. Since spinel and olivine tend to crystallise at, or close to, the liquidus in primitive melts the crystallisation temperature that they record approximates the liquidus temperature, which itself represents the minimum temperature of mantle melting (because melts could only have cooled since they were generated). This thermometry technique is considered robust to post-crystallisation diffusive resetting because the diffusion rate of Al in olivine is extremely slow at low silica activity (Spandler and O'Neill, 2010; Zhukova et al., 2017), and is ideally used when spinel crystals are trapped and isolated in a closed system within the olivine structure.

2.3 Analytical

In order to use the Al-in-olivine thermometer as calibrated by Wan et al. (2008) and Coogan et al. (2014), we measured the compositions of spinel inclusions and their olivine hosts by EPMA. The spinels are in the cores of olivine phenocrysts (Figure 1), and to gain a representative measurement of the equilibrium olivine composition in Paraná-Etendeka picrites and ferropicrites, we averaged three analytical points in the olivine that were measured in a triangular configuration around the inclusion.

Analyses were carried out on polished thin sections and mounts of olivine grains. Electron probe microanalysis (EPMA) was performed in wavelength-dispersive mode using a Cameca

SX100 at the University of Cambridge. Analyses were performed using a focused beam with an accelerating voltage of 15 or 20 kV and a current of 20 nA for olivine and 40 nA for spinel. Standards used were: Fe-Kα_1 on fayalite; Ni-Kα_1 on NiO; Si-Kα_1 and Ca-Kα_1 on diopside; Mg-Kα_1 on St. Johns olivine; Al-Kα_1 on corundum; Cr-Kα_1 on pure metal; Ti-Kα_1 on rutile. The PAP correction was used to convert k-ratios to concentrations. To increase the precision of the measurements of Al in olivine, Al was measured using a LTAP crystal and a long counting time. Measurements were made over three analytical sessions with the following variations in accelerating voltage, counting time for Al in olivine, and relative uncertainty of Al: 1) 20 kV, 30 s, relative $1\sigma_{Al} = 0.29$; 2) 15 kV, 60 s, relative $1\sigma_{Al} = 0.21$; and 3) 15 kV, 140 s, relative $1\sigma_{Al} = 0.14$ (labelled in Supplementary Table S1; counting times of other elements and for spinel measurements given in Supplementary Table S2). These uncertainties are propagated through temperature calculations.

The analytical points in olivine were measured approximately 20–30 μm from the inclusion edge. Given that Al is a major element in spinel and a trace element in olivine, there is a risk that the apparent Al_2O_3 concentration of the olivine ($Al_2O_3^{olivine}$) could be increased by secondary fluoresced X-rays from within the spinel inclusion (e.g. Borisova et al., 2018). We checked this with Monte Carlo simulations using PENEPMA (v. 2014; Llovet and Salvat, 2017), converting k-ratios to concentrations using CalcZAF (derived from CITZAF; Armstrong, 1995). In the simulation, a pure $MgAl_2O_4$ spinel half-sphere was set within pure Fo_{90} olivine. At various distances from the interface, the sample was bombarded with a simulated 15 keV electron beam for several hours to reach an arbitrary low uncertainty. An annular detector spanning a 35–45° take-off angle was used to represent the 40° take-off angle of a microprobe. We found that the fluoresced apparent Al_2O_3 signal from $MgAl_2O_4$ spinel dropped below 0.005 wt.% (became negligible) at around 4 μm from the edge of a 20 μm inclusion (Figure 2), although we caution that a much higher level of secondary fluorescence of Al is expected in the case of an olivine inclusion within a larger spinel crystal.

Spinel $Fe^{3+}/\Sigma Fe$ and Fe^{3+} per formula unit (p.f.u.) were initially calculated stoichiometrically from the EPMA data according to the method of Droop (1987) on the basis of four oxygens. Nine spinel standards, that had previously been characterised by Mössbauer and EPMA (Davis et al., 2017; Ionov and Wood, 1992; Wood and Virgo, 1989) and XANES, were analysed in the same analytical session: their $Fe^{3+}/\Sigma Fe$ was, on average, overestimated by a factor of 1.7, so the $Fe^{3+}/\Sigma Fe$ of the unknown spinels was multiplied by a correction factor of 0.6. The final Fe^{3+} values should therefore be considered approximate values only. However, they indicate that the spinel samples fall within the $Fe^{3+}/\Sigma Fe$ calibration range of the Al-in-olivine thermometer (Coogan et al., 2014; Wan et al., 2008).

In the study of Coogan et al. (2014), the thermometer reproduced the experimental temperatures of 42 of the 45 calibration experiments to within 20 °C, indicating an inherent 1σ uncertainty of the thermometer of 11 °C (note that this is lower than the uncertainty derived by propagating the errors of fit of the individual coefficients, which relates to correlation between those coefficients' uncertainties). In all cases, the analytical uncertainty in $Al_2O_3^{olivine}$ is greater than that of the thermometer, so we propagate this analytical uncertainty to define temperature uncertainties.

3 Results

3.1 Initial data filtering

The Al-in-olivine technique is appropriate for fairly primitive Cr–spinel and olivine pairs, and is calibrated using a limited range of spinel compositions. Spinel has solid solutions with a range of end-members: a high proportion of the spinel ($MgAl_2O_4$) and magnesiochromite ($MgCr_2O_4$) end-members are indicative of crystallisation from a more primitive melt, whereas increasing concentrations of Ti and Fe^{3+} in the B site, as well increasing Fe/Mg in the tetrahedral A site, are expected with melt evolution. Although most inclusions in the Paraná-Etendeka olivines were found to be rich in spinel/chromite-series components, several were rich in Ti and

Fe^{3+}, and a few inclusions in low-forsterite olivine were in fact ilmenite or magnetite. The data were therefore initially filtered, such that inclusion measurements where Al+Cr < 1.4 p.f.u. were discarded. The complete compositional data (excluding these low Al+Cr analyses) is provided in Supplementary Table S1.

3.2 Crystal chemistry and thermometer applicability

Measured olivine crystals with appropriate spinel inclusions had compositional ranges of Fo_{78}–Fo_{94} and 0.04–0.13 wt.% Al_2O_3 in the picrite samples, and Fo_{68}–Fo_{85} and 0.03–0.06 wt.% Al_2O_3 in the ferropicrite samples (Figure 3). The Ca contents in all olivines are relatively high (CaO = 0.25–0.35 wt. %), ruling out a mantle xenocryst origin (Thompson and Gibson, 2000; De Hoog et al., 2010). The thermometer indicates that olivines crystallised at higher temperatures will contain more Al_2O_3, so the generally positive correlation between Fo and $Al_2O_3^{olivine}$ shown in Figure 3 is expected. For the subset of olivines in which P_2O_5 was measured, the average concentration was below the detection limit, so corrections are not required for P–Al substitution (cf. Coogan et al., 2014). The activity of SiO_2 in the picrite and ferropicrite melts was likely low and similar to the calibration experiments, so little added uncertainty is expected from an additional silica + vacancy substitution mechanism (Coogan et al., 2014). In addition, $Al_2O_3^{olivine}$ may be affected by high TiO_2 activity because the incorporation of Ti into olivine octahedral sites could be charge-coupled with substitution of Si for Al in olivine tetrahedral sites. This would lead to anomalously high temperature estimates for olivine with high Ti concentrations, although alternative solution mechanisms for Ti in olivine also exist (Hermann et al., 2005). However, this is not considered to be a problem here as $TiO_2^{olivine}$ concentrations were close to, or below, detection limits of 0.01 to 0.03 wt.% (depending on setup).

Aspects of the spinel inclusion compositions are shown in Figure 4a and b. The range in spinel Cr# was 0.40–0.70 in the picrite samples and 0.45–0.63 in the ferropicrite samples. Fe^{3+} and Ti^{4+} in spinel need to be considered, because the presence of magnetite and ulvöspinel

components of spinel will affect the activity coefficients of aluminium and chromium end-members. The range of spinel Fe^{3+} (following the initial filtering described in section 3.1) is well within the limit of the thermometer calibration range, so does not pose a problem. However, the measured spinels reach higher Ti contents than the calibration set. This is particularly true of the ferropicrite spinels, because these magmas are relatively high in Ti (as shown by whole-rock measurements and melt inclusions; Gibson et al., 2000; Jennings et al., 2017). The extent to which high Ti contents will affect the thermometry results is uncertain, but we err on the side of caution and restrict our dataset to spinel–olivine pairs where the maximum spinel Ti content is not far from the maximum in the calibration dataset. An upper limit of 0.05 Ti p.f.u. was chosen for spinels in the picrite samples and corresponds to ~2 wt.% TiO_2. A higher limit of 0.08 p.f.u. (~3 wt. % TiO_2) is applied to the spinels in the ferropicrites. The corresponding temperatures are shown in Figure 4c and d, where the few high-temperature outliers in the picrite data are seen for spinels with high Ti contents. Data points above our stated limits were removed from the dataset for the subsequent results and discussion.

3.3 Crystallisation temperature

Histograms and Probability Distribution Functions (PDF) of calculated crystallisation temperatures are shown in Figure 5. The PDF curves incorporate the uncertainties in temperature estimates, which tend to be larger at lower temperatures because of the lower $Al_2O_3^{olivine}$ concentrations, resulting in a low-temperature tail. The mean equilibration temperature of all picrite spinel-olivine pairs is 1372±13 °C (1σ = 84°C; Figure 5a). However, the highest Fo olivines must have crystallised first and would record a temperature closer to the liquidus. The mean temperature for spinel-olivine pairs where olivine is $Fo_{>90}$ is therefore higher, at 1458 ± 11 °C (1σ = 36°C; Figure 5b). We consider this small group of ten measurements to approximate the liquidus temperature. The highest temperature estimate was obtained from an olivine ($Fo_{92.9}$) in sample 97SB33, with an equilibration temperature of 1511 °C (1σ = 24 °C). This is in stark

contrast to the range of equilibration temperatures obtained from olivine-inclusion MgO partitioning by Keiding et al. (2011, 2013) of 1279 – 1361 °C from samples of similar Horingbaai picrites with equally high Fo olivine. The lower temperatures obtained by Keiding et al. (2011, 2013) may reflect the higher mobility of Fe-Mg compared to Al during heating and rehomogenisation of the melt inclusions (see section 4.2.1).

The crystallisation temperatures of the olivines in the ferropicrite are generally lower than those of the picrites, which is somewhat expected given their lower Fo content (Roeder and Emslie, 1970). The mean equilibration temperature of ferropicrite spinel-olivine pairs is 1296 ± 7 °C (1σ = 29 °C; Figure 5c). Given the narrow spread in the data, we use this value to approximate the liquidus temperature of the ferropicrites. Primary ferropicrite liquids are Fe-rich (Gibson et al., 2000), so the lower Fo content of ferropicrite olivine does not imply significant fractionation.

We examine the temperature variations with olivine Fo content in Figure 6, in which the individual samples are shown in order to identify fractionation trends within them. Temperature and Fo are expected to decrease in tandem as a magma cools and fractionates. In the sample of Paraná-Etendeka picrites, a cluster of the highest Fo (>90), highest T (>1400 °C) measurements are clearly distinguishable: all samples except 97SB41 are represented within this cluster. A fractionation trend was modelled in Petrolog3 (Danyushevsky and Plechov, 2011). Calculations were performed assuming fractional crystallisation at 3 kbar at the FMQ oxygen buffer using the whole-rock composition of picrite sample 97SB33, corrected for olivine fractionation, as a starting composition (supplementary table S3). This trend, also shown in Figure 6, indicates that temperature should rapidly decrease at the onset of crystallisation, with a moderate decrease in Fo. After plagioclase and clinopyroxene saturate, temperature decreases more gently with Fo.

The high-temperature olivines in picrite sample 97SB41 crystallised at higher temperatures than can be related to the $Fo_{>90}$ cluster by simple fractional crystallisation. One possibility is that the spread in temperatures at a given Fo content reflects Fe-Mg re-equilibration: whereas Al

diffuses slowly in olivine, Fe–Mg exchange is relatively fast (e.g. Chakraborty, 1997). Fe–Mg exchange would cause forsterite content to decouple from Al-in-olivine temperatures. Sample 97SB41 has a narrow range of forsterite contents, and grains do not appear zoned in BSE images, so Fe–Mg interdiffusion may have reduced the forsterite content of olivine cores in the highest temperature grains. In contrast, 97SB33 preserves some zoning and a larger range in forsterite contents. Alternatively, the spread in data could be explained by crystallisation at different pressures, i.e. the macrocrysts in 97SB41 crystallised at higher pressure than in 97SB33. At higher pressures, olivines of similar forsterite content would crystallise at higher temperature. However, in order to match the temperature–forsterite trend of 97SB41 in Figure 6, pressures of around 20 kbar are required (according to Petrolog3 modelling, with all other variables as before). Such high pressure crystallisation is unlikely because i) 20 kbar is likely near to, or deeper than, the base of the lithosphere (see section 4.2), and ii) Petrolog3 predicts a 3:1 ratio of clinopyroxene to olivine to fractionate at 20 kbar to explain the high-temperature, low-forsterite measurements 97SB41, whereas petrographic evidence for early clinopyroxene crystallisation (e.g. macrocrysts) is lacking in this sample. Olivine ± plagioclase macrocrysts in the picrites are generally indicative of low pressure crystallisation. Finally, the variability could indicate crystallisation trends from distinct melts, where some (e.g. the primary melt from which 97SB41 derives) have a lower equilibrium olivine Fo (lower Mg/Fe) at a temperature that is almost as high as that of the high-Fo cluster. Variability in primary melt compositions is expected, and could in part arise from the mixing and accumulation of variably depleted mantle melts, which would have a range of Fe/Mg ratios (e.g. Shorttle and Maclennan, 2011), although mantle melts appear to have mixed rather efficiently prior to olivine crystallisation in these samples (Jennings et al., 2017).

In comparison to the temperatures recorded by olivine-spinel pairs from different samples of Paraná-Etendeka picrites, those for the ferropicrite are all within uncertainty of one-another. The highest temperature is 1346 °C (1σ = 54 °C), which surprisingly comes from a rather low Fo

(Fo_{74}) olivine. It is not clear to what extent the lack of a clear trend beyond a weak positive correlation between Fo and *T* in the ferropicrites results from: (i) fractionation; (ii) magma mixing between primary melts with significant variations in Fe/Mg; and/or (iii) mixing with more evolved magmas; or (iv) is simply related to thermometer shortcomings with these unusual compositions.

4 Discussion

4.1 Comparison with global dataset of Al-in olivine crystallisation temperatures

Crystallisation temperatures from high-Fo olivines have been reported from a range of plume-related settings. Barring Iceland, these are all continental flood basalts (CFBs) or other LIPs, and thus are comparable with the Paraná-Etendeka CFB province in terms of tectonic setting and potentially derive from melting within upwelling mantle thermal anomalies. We compare the frequency distribution of Etendeka olivine-spinel crystallisation temperatures with a global compilation of those from other plume-related provinces in Figure 7a. The hottest known crystallisation temperatures from Al-in-olivine thermometry are from Tortugal, part of the Caribbean Large Igneous Province (Trela et al., 2017), and these stand out in Figure 7a as clearly representing exceptionally high temperature melts in the Phanerozoic. These measurements are derived from correspondingly forsteritic olivine of up to $Fo_{94.2}$. Figure 7a shows that the Paraná-Etendeka olivine-spinel pairs record very high temperatures even amongst comparable LIPs, and the high temperature tail of the distribution indicates near-liquidus crystallisation temperatures that are amongst the hottest of all LIP samples (excluding the CLIP samples). For comparison, the 95th percentile of Paraná-Etendeka picrite crystallisation temperatures is at 1484 °C, which is similar to olivine–spinel temperatures estimated for the Karoo and North Atlantic Igneous CFB provinces but >100 °C hotter than reported for the Emeishan CFB province and Iceland (Coogan et al., 2014; Heinonen et al., 2015; Matthews et al., 2016; Spice et al., 2016; Xu and Liu, 2016; Table 1). This provides strong evidence for a pronounced thermal anomaly in the mantle source

of the Paraná-Etendeka CFB province.

Table 1 Mean reported olivine–spinel equilibrium temperature, the temperature at the 95th percentile, and the number of measurements. References as for Figure 7.

Type	Province	*n*	Mean *T* (°C)	P_{95} (°C)
MORB		30	1193	1254
Ice-land**		101	1288	1368
LIP	CLIP	81	1427	1568
	Emeishan	48	1280	1379
	Etendeka*	40	1372	1484
	Karoo	21	1357	1474
	Madagascar	5	1334	1459
	NAIP	114	1393	1474

*excluding ferropicrites

** including Tertiary Icelandic samples from Spice et al. (2016)

More generally, Figure 7b shows PDFs of Al-in-olivine temperatures for samples from different tectonic setting. The bandwidth is related to typical analytical uncertainties. It is clear that there is a large offset in the highest probability (the mode) temperature of approximately 100 °C between MORB, Iceland and CFBs. Interestingly, the CFB distribution appears to be bimodal; this may be due to sampling bias but it is apparent that samples from CFB provinces have a probability tail that extends to much higher temperatures than MORB and Iceland. The maximum olivine temperatures recorded are the closest to the liquidus of the primary melt, so we can consider the high temperature limits of these distributions (or the 95th percentile temperature to reduce bias from low sampling rates; Table 1). The 95th percentile temperatures for different

CFB provinces range from 1379 to 1568 °C, which represents an offset from MORB of 125–314 °C, implying a much hotter mantle source.

4.2 Potential temperature in the proto-Tristan mantle plume from the Etendeka picrites

The potential temperature of the mantle *must* be higher than the crystallisation temperature because of the enthalpy of fusion and adiabatic cooling. MORB forms from decompression melting of ambient mantle with a T_P of around 1315 –1350 °C (e.g. Herzberg et al., 2007; Katz et al., 2003; Matthews et al., 2016; McKenzie et al., 2005; White and McKenzie, 1989); the discrepancy between these studies and the higher temperature estimate of ~1450 °C from the method of Putirka et al. (2007) is discussed by Matthews et al. (2016). Crystallisation temperatures of up to ~ 1600 °C in CFB provinces are, therefore, clear evidence of mantle thermal anomalies of > 200 °C, even without using assumptions to relate crystallisation temperature to mantle T_P.

In order to calculate the T_P of the mantle source of the picrites in the Paraná-Etendeka from the crystallisation temperature, we must reconstruct the thermal pathway from melt generation through to crustal emplacement. The method used here is similar, but not identical, to that used by Matthews et al. (2016), who determined a T_P of 1480 °C for the mantle source of recent Icelandic melts by calculating the thermal pathway of the melts from source to emplacement. We calculate this with the assumption that the mantle source of the Etendeka picrites is a KLB1-like peridotite; this is supported by major element, trace element and isotope geochemistry (Jennings et al., 2016; Thompson et al., 2001).

Assuming that the spinel-olivine equilibrium temperature is at or below the liquidus, we can use the liquidus temperature (taken to be the average of the $Fo_{>90}$ olivine temperatures, 1458 °C), to constrain a minimum crustal emplacement temperature, and so a minimum mantle T_P for the Paraná-Etendeka picrites. We then produce a forward model of decompression, melting, and the cessation of melting at the base of the lithosphere, and allow the T_P to vary until the predicted

emplacement temperature matches this Al-in-olivine temperature.

The thermal model and parameters used here are the peridotite model of Jennings et al. (2016), which is based on the equations and method of Katz et al. (2003) but uses an updated parameterisation of KLB-1 peridotite melting based on Holland and Powell (2011) and Jennings and Holland (2015). This assumes that upwelling peridotite follows an adiabat (that defines T_P) and then intersects the solidus. Following this, the enthalpy of fusion further reduces the temperature during batch decompression melting: the melt and residue are assumed to maintain thermal equilibrium. Whilst this assumption represents a simplification, the timescales of thermal equilibration are much shorter than those of mass transfer required for chemical equilibrium, and the temperature and chemical properties of fractional melts can become decoupled, as discussed by Matthews et al. (2016). The appropriateness of the equilibrium assumption was tested by Jennings et al. (2016), who found limited divergence between incremental batch melting and equilibrium melting thermal pathways.

Melting ceases once upwelling material reaches the base of the lithosphere: at this point the liquid is assumed to segregate from the solid and follows a basaltic liquid adiabat to the pressure of the magma chamber in which it is emplaced. An example of a calculated thermal path is shown in Figure 8.

The results for the best fit T_P required to reproduce a given liquidus temperature (in this case 1458 °C) are dependent upon lithospheric thickness (because the lithospheric thickness dictates the shallow limit to melting and thus melt fraction F) and crystallisation pressure (P_{cryst}). The picrites were generated during a period of rifting and lithospheric thinning associated with the opening of the Atlantic Ocean. The lithospheric thickness at the time of picrite generation has been estimated from REE inversion techniques to be around 50 km depth (Thompson et al., 2001; Thompson and Gibson, 2000). To understand how different lithospheric thicknesses might affect the calculated T_P required to match the picrite crystallisation temperatures, we performed the calculations over a complete range of lithospheric thickness, corresponding to the pressure

just above the peridotite solidus (125 km or 112 km to match the melt temperature emplaced at 10 or 5 kbar, respectively) through to the emplacement pressure (30 or 15 km; Figure 9). We find that the calculated T_P is fairly insensitive to lithospheric thickness (and therefore also F), varying by <100 °C over the entire lithospheric thickness range.

The effect of the assumed crystallisation pressure on the calculated T_P is moderate, where T_P calculated at P_{cryst} = 1.0 GPa tends to be around 50 °C cooler than that calculated at P_{cryst} = 0.5 GPa. 0.5 GPa is consistent with the co-saturation of olivine and plagioclase feldspar in these samples (Thompson et al., 2001) and with an average pressure of 5.3 kbar from clinopyroxene thermobarometry of five Horingbaai picrite samples (Keiding et al., 2013; barometer uncertainty ± 1.3 kbar, Putirka, 2008). At the previously suggested lithospheric thickness of 50 km and a crystallisation pressure of 0.5 GPa, we find a T_P of 1623^{+22}_{-20} °C (F = 0.33). The stated uncertainty is derived from the standard error of the mean crystallisation temperature of 11 °C. Taking uncertainties into account, our preferred range of T_P solutions for the Paraná-Etendeka mantle source is approximately 1600–1640 °C. The possible T_P solutions across the entire range of parameter space is around 1550–1675 °C, excluding a spike where clinopyroxene becomes exhausted from the residue close to the base of the lithosphere (Figure 9). For comparison, Matthews et al. (2016) used a similar method to calculate a T_P of 1480 °C for the Iceland mantle plume from the olivine-spinel crystallisation temperatures shown in Figure 7b.

The T_P of the ferropicrite mantle source is more difficult to calculate due to the uncertainty of the inferred pyroxenite composition, mineralogy, thermodynamic properties and melt productivity (Gibson, 2002; Jennings et al., 2016; Tuff et al., 2005). In addition, an unknown water or other volatile content may somewhat depress the pyroxenite solidus.

Silica-undersaturated mantle pyroxenite is thought to form by either solid-state hybridisation of subducted crust (i.e. eclogite) with peridotite, or through the reaction of eclogite-derived partial melts with peridotite (e.g. Yaxley and Green, 1998; Herzberg et al., 2011); previous studies on pyroxenite melting have tended to consider starting materials with a chemistry that

reflect these processes. Jennings et al. (2016) used thermodynamic modelling to investigate the composition of the partial melts of the anhydrous 50:50 peridotite-basalt hybrid composition (KG1-like, after of Kogiso et al., 1998), and found that low-fraction melts produced at elevated T_P were broadly similar to the Etendeka ferropicrites. Given that we have little additional information available about the exact composition and origin of pyroxenite in the Etendeka mantle source, we have chosen to use that same composition to represent pyroxenite melting in the present study. We simplify the modelling by assuming a single hybrid lithology, and disregard the effect of heat transfer between heterogeneous lithologies (cf. Phipps Morgan, 2001).

The uncertainty in pyroxenite composition and melting behaviour add to that introduced by the unknown effect of the high Ti content of the ferropicritic spinels on the thermometer accuracy. For these reasons, a ferropicrite mantle source estimation should be considered an approximate value only.

We use the properties and melting characteristics parameterised by Jennings et al. (2016) of a KG1-like composition to approximately model the thermal pathway of pyroxenite partial melts, employing the same method as described for peridotite melting. For the mean crystallisation temperature of 1296 °C, we find T_P solutions of 1360–1500 °C for the permissible ranges of lithospheric thickness at our preferred crystallisation pressure of 1.0 GPa (Gibson et al., 2000). This increases to 1360–1550 °C if crystallisation occurred at 0.5 GPa. While these values are only approximate, and are limited by the stated caveats, they do appear to indicate that the ferropicrites were derived from mantle that was somewhat cooler than the picrite source, but warmer than ambient mantle. One plausible explanation is that the pyroxenite source of the ferropicrites was entrained within the upwelling head of the proto-Tristan plume. Alternatively, pyroxenite may have been present in the cooler peripheries of the plume head, but because pyroxenite is expected to be denser than peridotite in the mantle, this is more difficult to reconcile with the requirement for buoyancy.

4.2.1 Comparison with previous T_P estimates of the proto-Tristan plume

The MgO content of any primary mantle melt should be directly related to mantle T_P and the extent of melting (F), and simple parameterisations of this relationship have been proposed (e.g. Herzberg et al., 2007). It is therefore unsurprising that debate has focused on the method of deducing the primary melt MgO. Previous estimates of magmatic temperatures and T_P of primitive magmas from the Paraná-Etendeka CFB province have been based on the Fo content (so the Fe/Mg ratio) of olivine, which preserves a more reliable record of the primary melt than whole-rock composition.

Thompson and Gibson (2000) examined some of the same samples as our study: their highest temperatures are also obtained from sample 97SB33, which contains the most forsteritic olivines in the collection (up to $Fo_{93.3}$). In order to calculate T_P, Thompson and Gibson (2000) first calculated an equilibrium melt Mg/(Mg+Fe) content by using a pressure-dependent Fe-Mg exchange coefficient ($K_{D\,\mathrm{Fe\text{-}Mg}}^{\mathrm{ol\text{-}liq}}$), then deduced the melt MgO content by extrapolating from whole-rock MgO vs. Mg/(Mg+Fe) relationships. This gave calculated melt MgO contents in excess of the whole-rock MgO concentrations, indicating a komatiitic parental melt with 24 wt.% MgO and a correspondingly high T_P of ~ 1680 °C. This implies that the olivine macrocrysts were transported by a lower MgO melt than the envisaged hot dense komatiitic melt from which they grew. This method and interpretation were, however, later disputed by Keiding et al. (2011). Using picrite samples from the same localities, Keiding et al. (2011) took the alternative approach of measuring MgO directly from olivine-hosted melt inclusions. They found far lower MgO concentrations of up to 17.5 wt. %, requiring a maximum T_P of 1520 °C and negating the requirement for a komatiitic origin for the high-Fo macrocrysts. Whilst they make a reasonable point that it is difficult to infer MgO content from olivine composition alone, Keiding et al. (2011) failed to account for the difficulties in using the major element composition, and in particular the FeO and MgO concentrations, of rehomogenised olivine-hosted melt inclusions.

The melt FeO and MgO can rapidly undergo diffusive re-equilibration with the host olivine during heating in a furnace, which will: (i) alter their concentrations in a way that cannot be easily corrected for; and (ii) result in MgO concentrations that tend towards equilibrium according to the furnace temperature (Jennings et al., 2017). The MgO contents measured by Keiding et al. (2011) correspond to Fo-MgO equilibrium temperatures of 1246 to 1395 °C (rehomogenised at 1350 °C).

The T_P range suggested by our Al-in-olivine thermometry study of 1600–1640 °C is very high even by the standards of all other Phanerozoic LIPs (except for CLIP; Trela et al., 2017) and lies between the estimates of Thompson and Gibson (2000) and Keiding et al. (2011). We stress that the different thermometry methodologies used by Thompson and Gibson (2000), Keiding et al. (2011), and in our present investigation, all point to significantly elevated T_P in the Parana-Etendeka CFB mantle source: they only disagree on the exact size of that temperature offset from ambient. Our high temperature and associated high F are supported by generally depleted incompatible trace element compositions, both in whole-rock samples and olivine-hosted melt inclusions (Jennings et al., 2017; Keiding et al., 2011; Thompson et al., 2001). This high T_P of the Tristan plume starting head contrasts with the lower estimated T_P of around 1360 °C for the modern-day Tristan hotspot (Weit et al., 2017). These estimates were also made using olivine-melt Mg exchange thermometry, using both bulk rock and olivine-hosted melt inclusion compositions. If the lower apparent T_P is not related to the different thermometry material used, it indicates a significant cooling of the plume through time.We suggest that using the Al-in-olivine thermometer to estimate of crystallisation temperatures is more robust than Fe–Mg exchange-based methods, although the weakness still resides in the assumptions required to convert crystallisation temperature to T_P, making the crystallisation temperature more certain than its source temperature.

4.2.2 Comparison with T_P estimates based on melt composition and parameterisations of mantle melting

An alternative method for determining T_P is to not consider olivine-melt exchange thermometry at all; rather, the major element composition of a melt can directly be compared to parameterisations of peridotite melting. PRIMELT3 (Herzberg and Asimow, 2015) uses a parameterisation based on adiabatic melting paths calculated in pMELTS (Ghiorso et al., 2002). By adding olivine that had been lost through fractionation, we create a corrected form of composition 97SB33, where olivine is in equilibrium with the melt (K_D = 0.31; composition in Supplementary Table S3). PRIMELT3 modelling suggests that this composition derives from around 3% olivine fractionation of primary magma composition with 17.7 wt.% MgO, which itself can be explained by around 26 % partial melting of peridotitic mantle with a T_P of 1505 °C. This estimate of T_P is somewhat lower than that derived from modelling of Al-in-olivine thermometry results, which may in part be explained by different uncertainties associated with the two methods, including differences in the underlying thermodynamic models. However, we emphasize that two completely independent methods of estimating T_P (olivine-spinel Al-exchange vs. applying empirical parameterisations to melt major element compositions) both point towards the same conclusion: that the Paraná-Etendeka CFB mantle source was significantly hotter, by hundreds of degrees, than ambient mantle.

5 Conclusions

Al-in-olivine thermometry provides an alternative method to traditional Mg-Fe-based techniques to assess crystallisation temperatures in primitive melts, with the advantages that: (i) no assumptions need to be made about the equilibrium melt composition; and (ii) the thermometry is more robust to diffusive resetting in slow cooling scenarios (Coogan et al., 2014; Wan et al., 2008). The EPMA technique is ideal for making the required spinel and olivine measurements because of both its high spatial resolution and ability to measure trace element

concentrations down to 10s –100s ppm for some elements. We have demonstrated that secondary fluorescence from Al in small spinel inclusions (< 20 μm) will have a negligible effect on typical Al concentrations measured in olivine at 15 kV, provided that measurements are made at a minimum distance of least ~4 μm from the interface. However, contamination of the olivine measurement by fluorescence will increase for larger grains or higher accelerating voltages, increasing the corresponding minimum distance from the spinel-olivine interface required for an accurate measurement.

Crystallisation temperatures based on the Al-in-olivine thermometer for picrites from the Paraná-Etendeka CFB province reach up to 1511 °C (1σ = 24 °C; $Fo_{92.9}$) with a mean of 1458±11 °C for 11 measurements obtained for olivine with $Fo_{>90}$. By contrast, the precursor ferropicrites have a maximum olivine-spinel co-crystallisation temperature of 1346 °C (1σ = 53 °C) and an average temperature of 1296±7 °C. The lower temperature estimates for the most primitive ferropicrites indicate that their pyroxenitic mantle source was somewhat cooler than the picrite source, and could be explained by the entrainment of pyroxenite by the upwelling head of the proto-Tristan plume or the presence of pyroxenite in the cooler peripheries of the plume.

Given that olivine and spinel would co-saturate at, or close to, the liquidus, the highest crystallisation temperatures are interpreted to represent the minimum temperature of the liquidus, which in turn represents a minimum temperature of the melt during emplacement in a crustal magma reservoir. We assign a minimum liquidus temperature for the picrites of 1458 °C, which is around 100–150 °C hotter than the T_P of ambient mantle. We converted the crystallisation temperature of magmas from the Paraná-Etendeka CFB to a mantle T_P by forward-modelling the *PT* path of decompression melting by assuming a peridotite source composition and using the equilibrium melting method of Katz et al. (2003) and the melting parameterisation of Jennings et al. (2016). The T_P required to match the liquidus temperature slightly depends on the assumed thickness of the lithosphere as well as the depth of emplacement: for the Paraná-Etendeka

picrites the best estimate of these parameters based on previous studies (around 50 km lithospheric thickness and 0.5 GPa emplacement pressure) results in a T_P estimate of 1623^{+22}_{-2} °C, corresponding to a high melt fraction of 0.33. This represents a significant thermal anomaly relative to ambient mantle of around +300 °C, and is extremely hot, even by CFB standards: the only higher crystallisation temperatures and interpreted mantle T_P in Phanerozoic primitive magmas have been found in the CLIP province (Trela et al., 2017). For comparison, the 95th percentile crystallisation temperature for the Karoo and NAIP are almost as high as the Etendeka picrites (1484 °C); whereas those from the Emeishan CFB province (1379 °C) are much lower.

The very high temperature estimates that we report for the proto-Tristan mantle plume starting head are intermediate between those estimated by Fe-Mg-based methods, being somewhat lower than estimates based on a calculated liquid composition (T_P = 1680 °C; Thompson and Gibson, 2000), and higher than methods based on melt inclusions (T_P = 1520 °C; Keiding et al., 2011). Such high crystallisation temperatures and mantle potential temperature estimates, together with $^3He/^4He$ ratios up to 10 times R_A (Stroncik et al., 2017) in the Paraná-Etendeka picrites are consistent with conceptual models that invoke a mantle plume starting head in their generation, as well as in the generation of other comparable CFB provinces. Measurements of a more recently-erupted sample from the Tristan mantle plume indicate a cooler T_P of around 1440 °C (Herzberg and Asimow, 2008), which is broadly consistent with estimates of the mantle around Tristan da Cuhna of T_P = 1410–1430 °C from inversion of seismic velocities from an ocean-bottom seismometer array (Bonadio et al., 2018): our results therefore support a model of secular cooling of the Tristan mantle plume.

6 Acknowledgements

We would like to thank Iris Buisman for technical support during the EPMA measurements, as well as for producing the QEMSCAN images. We are grateful to Godfrey Fitton, Claude

Herzberg and Lawrence Coogan for their careful and insightful reviews that led to improvements of this manuscript, and to Catherine Chauvel for editorial handling. We also thank Simon Matthews, Lucy Tweed and Oliver Shorttle for useful discussion throughout the project. We acknowledge the scientists involved in the field expeditions during which samples used in this study were collected including: Bob Thompson, Paula Antoshechkina, Teal Riley, Philip Leat and Ilona Romu. This work was supported by a Natural Environment Research Council studentship [NE/J500070/1 to E.S.J.].

7 Supplementary information

Supplementary Table S1: Complete dataset

Supplementary Table S2: EPMA counting times

Supplementary Table S3: Starting composition for Petrolog3 model

Supplementary Figure S1: Map of sample localities

Supplementary Figure S2: QEMSCAN images

8 References

Armstrong, J.T., 1995. CITZAF: a package of correction programs for the quantitative Electron Microbeam X-Ray-Analysis of thick polished materials, thin-films, and particles. Microbeam Anal. 4, 177–200.

Arndt, N.T., Czamanske, G.K., Wooden, J.L., Fedorenko, V.A., 1993. Mantle and crustal contributions to continental flood volcanism. Tectonophysics 223, 39–52. https://doi.org/10.1016/0040-1951(93)90156-E

Beattie, P., 1993. Olivine-melt and orthopyroxene-melt equilibria. Contrib. Mineral. Petrol. 115, 103–111. https://doi.org/10.1007/BF00712982

Bonadio, R., Geissler, W.H., Lebedev, S., Fullea, J., Ravenna, M., Celli, N.L., Jokat, W., Jegen, M., Sens-Schönfelder, C., Baba, K., 2018. Hot Upper Mantle Beneath the Tristan da

Cunha Hotspot From Probabilistic Rayleigh-Wave Inversion and Petrological Modeling. Geochem. Geophys. Geosystems 19, 1412–1428. https://doi.org/10.1002/2017GC007347

Borisova, A.Y., Zagrtdenov, N.R., Toplis, M.J., Donovan, J.J., Llovet, X., Asimow, P.D., de Parseval, P., Gouy, S., 2018. Secondary fluorescence effects in microbeam analysis and their impacts on geospeedometry and geothermometry. Chem. Geol. 490, 22–29. https://doi.org/10.1016/j.chemgeo.2018.05.010

Chakraborty, S., 1997. Rates and mechanisms of Fe-Mg interdiffusion in olivine at 980°–1300°C. J Geophys Res-Sol Ea 102, 12317–12331. https://doi.org/10.1029/97JB00208

Coogan, L.A., Saunders, A.D., Wilson, R.N., 2014. Aluminum-in-olivine thermometry of primitive basalts: Evidence of an anomalously hot mantle source for large igneous provinces. Chem. Geol. 368, 1–10. https://doi.org/10.1016/j.chemgeo.2014.01.004

De Hoog, J.C.M., Gall, L., Cornell, D.H., 2010. Trace-element geochemistry of mantle olivine and application to mantle petrogenesis and geothermobarometry. Chemical Geology 270, 196–215. https://doi.org/10.1016/j.chemgeo.2009.11.017

Danyushevsky, L.V., Plechov, P., 2011. Petrolog3: Integrated software for modeling crystallization processes. Geochem. Geophys. Geosystems 12, Q07021. https://doi.org/10.1029/2011GC003516

Davis, F.A., Cottrell, E., Birner, S.K., Warren, J.M., Lopez, O.G., 2017. Revisiting the electron microprobe method of spinel-olivine-orthopyroxene oxybarometry applied to spinel peridotites. Am. Mineral. 102, 421–435. https://doi.org/10.2138/am-2017-5823

Droop, G.T.R., 1987. A general equation for estimating Fe3+ concentrations in ferromagnesian silicates and oxides from microprobe analyses, using stoichiometric criteria. Mineral. Mag. 51, 431–435.

Erlank, A.J., Marsh, J.S., Duncan, A.R., Miller, R.M., Hawkesworth, C.J., Betton, P.J., Rex, D.C., 1984. Geochemistry and petrogenesis of the Etendeka volcanic rocks from SWA/Namibia, in: Petrogenesis of the Volcanic Rocks of the Karoo Province, Geological

Society of South Africa: Special Publication. Geological Society of South Africa, pp. 195–245.

Gibson, S.A., 2002. Major element heterogeneity in Archean to Recent mantle plume starting-heads. Earth Planet. Sci. Lett. 195, 59–74. https://doi.org/10.1016/S0012-821X(01)00566-0

Gibson, S.A., Thompson, R.N., Dickin, A.P., 2000. Ferropicrites: geochemical evidence for Fe-rich streaks in upwelling mantle plumes. Earth Planet. Sci. Lett. 174, 355–374. https://doi.org/10.1016/S0012-821X(99)00274-5

Heinonen, J.S., Jennings, E.S., Riley, T.R., 2015. Crystallisation temperatures of the most Mg-rich magmas of the Karoo LIP on the basis of Al-in-olivine thermometry. Chem. Geol. 411, 26–35. https://doi.org/10.1016/j.chemgeo.2015.06.015

Hermann, J., O'Neill, H.S.C., Berry, A.J., 2005. Titanium solubility in olivine in the system TiO2–MgO–SiO2: no evidence for an ultra-deep origin of Ti-bearing olivine. Contrib. Mineral. Petrol. 148, 746–760. https://doi.org/10.1007/s00410-004-0637-4

Herzberg, C., 2011. Identification of source lithology in the Hawaiian and Canary Islands: Implications for origins. J. Petrology 52, 113–146. https://doi.org/10.1093/petrology/egq075

Herzberg, C., Asimow, P.D., 2008. Petrology of some oceanic island basalts: PRIMELT2.XLS software for primary magma calculation. Geochem. Geophys. Geosystems 9, Q09001. https://doi.org/10.1029/2008GC002057

Herzberg, C., Asimow, P.D., 2015. PRIMELT3 MEGA.XLSM software for primary magma calculation: Peridotite primary magma MgO contents from the liquidus to the solidus. Geochem. Geophys. Geosystems 16, 563–578. https://doi.org/10.1002/2014GC005631

Herzberg, C., Asimow, P.D., Arndt, N., Niu, Y., Lesher, C.M., Fitton, J.G., Cheadle, M.J., Saunders, A.D., 2007. Temperatures in ambient mantle and plumes: Constraints from basalts, picrites, and komatiites. Geochem. Geophys. Geosystems 8, Q02006.

https://doi.org/10.1029/2006GC001390

Holland, T.J.B., Powell, R., 2011. An improved and extended internally consistent thermodynamic dataset for phases of petrological interest, involving a new equation of state for solids. J. Metamorph. Geol. 29, 333–383. https://doi.org/10.1111/j.1525-1314.2010.00923.x

Ionov, D.A., Wood, B.J., 1992. The oxidation state of subcontinental mantle: oxygen thermobarometry of mantle xenoliths from central Asia. Contrib. Mineral. Petrol. 111, 179–193. https://doi.org/10.1007/BF00348950

Jennings, E.S., Gibson, S.A., Maclennan, J., Heinonen, J.S., 2017. Deep mixing of mantle melts beneath continental flood basalt provinces: Constraints from olivine-hosted melt inclusions in primitive magmas. Geochim. Cosmochim. Acta 196, 36–57. https://doi.org/10.1016/j.gca.2016.09.015

Jennings, E.S., Holland, T.J.B., 2015. A simple thermodynamic model for melting of peridotite in the system NCFMASOCr. J. Petrol. 56, 869–892. https://doi.org/10.1093/petrology/egv020

Jennings, E.S., Holland, T.J.B., Shorttle, O., Maclennan, J., Gibson, S.A., 2016. The Composition of Melts from a Heterogeneous Mantle and the Origin of Ferropicrite: Application of a Thermodynamic Model. J. Petrol. 57, 2289–2310. https://doi.org/10.1093/petrology/egw065

Katz, R.F., Spiegelman, M., Langmuir, C.H., 2003. A new parameterization of hydrous mantle melting. Geochem. Geophys. Geosystems 4, 1073. https://doi.org/10.1029/2002GC000433

Keiding, J., Trumbull, R., Veksler, I., Jerram, D., 2011. On the significance of ultra-magnesian olivines in basaltic rocks. Geology 39, 1095–1098. https://doi.org/10.1130/G32214.1

Keiding, J.K., Frei, O., Renno, A.D., Veksler, I.V., Trumbull, R.B., 2013. Conditions of magma crystallization in the Henties Bay-Outjo dyke swarm, Namibia: Implications for the

feeder system of continental flood basalts. Lithos 179, 16–27. https://doi.org/10.1016/j.lithos.2013.07.018

Kogiso, T., Hirose, K., Takahashi, E., 1998. Melting experiments on homogeneous mixtures of peridotite and basalt: application to the genesis of ocean island basalts. Earth Planet. Sci. Lett. 162, 45–61. https://doi.org/10.1016/S0012-821X(98)00156-3

Langmuir, C.H., Klein, E.M., Plank, T., 1992. Petrological systematics of mid-ocean ridge basalts: Constraints on melt generation beneath ocean ridges, in: Morgan, J.P., Blackman, D.K., Sinton, J.M. (Eds.), Geophysical Monograph Series. American Geophysical Union, Washington, D. C., pp. 183–280.

Llovet, X., Salvat, F., 2017. PENEPMA: A Monte Carlo Program for the Simulation of X-Ray Emission in Electron Probe Microanalysis. Microsc. Microanal. 23, 634–646. https://doi.org/10.1017/S1431927617000526

Marsh, J.S., Ewart, A., Milner, S.C., Duncan, A.R., Miller, R.M., 2001. The Etendeka Igneous Province: Magma types and their stratigraphic distribution with implications for the evolution of the Paraná-Etendeka flood basalt province. Bull. Volcanol. 62, 464–486. https://doi.org/10.1007/s004450000115

Matthews, S., Shorttle, O., Maclennan, J., 2016. The temperature of the Icelandic mantle from olivine-spinel aluminum exchange thermometry. Geochem. Geophys. Geosystems 17, 4725–4752. https://doi.org/10.1002/2016GC006497

McKenzie, D., Bickle, M.J., 1988. The volume and composition of melt generated by extension of the lithosphere. J. Petrol. 29, 625–679. https://doi.org/10.1093/petrology/29.3.625

McKenzie, D., Jackson, J., Priestley, K., 2005. Thermal structure of oceanic and continental lithosphere. Earth Planet. Sci. Lett. 233, 337–349. https://doi.org/10.1016/j.epsl.2005.02.005

Morgan, W.J., 1971. Convection plumes in the lower mantle. Nature 230, 42–43. https://doi.org/10.1038/230042a0

Neave, D.A., Buisman, I., Maclennan, J., 2017. Continuous mush disaggregation during the long-lasting Laki fissure eruption, Iceland. American Mineralogist 102, 2007–2021. https://doi.org/10.2138/am-2017-6015CCBY

Parsons, B., Sclater, J.G., 1977. An analysis of the variation of ocean floor bathymetry and heat flow with age. J. Geophys. Res. 82, 803–827. https://doi.org/10.1029/JB082i005p00803

Peate, D.W., 1997. The Paraná-Etendeka province. Geophys. Monogr. Am. Geophys. Union 100, 217–246.

Phipps Morgan, J., 2001. Thermodynamics of pressure release melting of a veined plum pudding mantle. Geochemistry, Geophysics, Geosystems 2, 2000GC000049. https://doi.org/10.1029/2000GC000049

Putirka, K.D., 2008. Thermometers and barometers for volcanic systems. Rev. Mineral. Geochem. 69, 61–120. https://doi.org/10.2138/rmg.2008.69.3

Putirka, K.D., Perfit, M., Ryerson, F.J., Jackson, M.G., 2007. Ambient and excess mantle temperatures, olivine thermometry, and active vs. passive upwelling. Chem. Geol. 241, 177–206. https://doi.org/10.1016/j.chemgeo.2007.01.014

Renne, P.R., Sprain, C.J., Richards, M.A., Self, S., Vanderkluysen, L., Pande, K., 2015. State shift in Deccan volcanism at the Cretaceous-Paleogene boundary, possibly induced by impact. Science 350, 76–78. https://doi.org/10.1126/science.aac7549

Richards, M.A., Duncan, R.A., Courtillot, V.E., 1989. Flood basalts and hot-spot tracks: Plume heads and tails. Science 246, 103–107. https://doi.org/10.1126/science.246.4926.103

Roeder, P.L., Emslie, R.F., 1970. Olivine-liquid equilibrium. Contrib. Mineral. Petrol. 29, 275–289. https://doi.org/10.1007/BF00371276

Saunders, A.D., 2016. Two LIPs and two Earth-system crises: the impact of the North Atlantic Igneous Province and the Siberian Traps on the Earth-surface carbon cycle. Geol. Mag. 153, 201–222. https://doi.org/10.1017/S0016756815000175

Shorttle, O., Maclennan, J., 2011. Compositional trends of Icelandic basalts: Implications for

short–length scale lithological heterogeneity in mantle plumes. Geochem. Geophys. Geosyst. 12, Q11008. https://doi.org/10.1029/2011GC003748

Sobolev, S.V., Sobolev, A.V., Kuzmin, D.V., Krivolutskaya, N. a., Petrunin, A.G., Arndt, N.T., Radko, V. a., Vasiliev, Y.R., 2011. Linking mantle plumes, large igneous provinces and environmental catastrophes. Nature 477, 312–316. https://doi.org/10.1038/nature10385

Song, H., Wignall, P.B., Tong, J., Yin, H., 2013. Two pulses of extinction during the Permian–Triassic crisis. Nat. Geosci. 6, 52–56. https://doi.org/10.1038/ngeo1649

Spandler, C., O'Neill, H.C., 2010. Diffusion and partition coefficients of minor and trace elements in San Carlos olivine at 1,300°C with some geochemical implications. Contrib. Mineral. Petrol. 159, 791–818. https://doi.org/10.1007/s00410-009-0456-8

Spice, H.E., Fitton, J.G., Kirstein, L.A., 2016. Temperature fluctuation of the Iceland mantle plume through time. Geochem. Geophys. Geosystems 17, 243–254. https://doi.org/10.1002/2015GC006059

Stroncik, N.A., Trumbull, R.B., Krienitz, M.-S., Niedermann, S., Romer, R.L., Harris, C., Day, J., 2017. Helium isotope evidence for a deep-seated mantle plume involved in South Atlantic breakup. Geology 45, 827–830. https://doi.org/10.1130/G39151.1

Thompson, R.N., Gibson, S.A., 2000. Transient high temperatures in mantle plume heads inferred from magnesian olivines in Phanerozoic picrites. Nature 407, 502–506. https://doi.org/10.1038/35035058

Thompson, R.N., Gibson, S.A., Dickin, A.P., Smith, P.M., 2001. Early Cretaceous basalt and picrite dykes of the southern Etendeka region, NW Namibia: Windows into the role of the Tristan mantle plume in Paraná–Etendeka magmatism. J. Petrol. 42, 2049–2081. https://doi.org/10.1093/petrology/42.11.2049

Trela, J., Gazel, E., Sobolev, A.V., Moore, L., Bizimis, M., Jicha, B., Batanova, V.G., 2017. The hottest lavas of the Phanerozoic and the survival of deep Archaean reservoirs. Nat. Geosci. 10, 451–456. https://doi.org/10.1038/ngeo2954

Tuff, J., Takahashi, E., Gibson, S.A., 2005. Experimental constraints on the role of garnet pyroxenite in the genesis of high-Fe mantle plume derived melts. J. Petrol. 46, 2023–2058. https://doi.org/10.1093/petrology/egi046

Wan, Z., Coogan, L.A., Canil, D., 2008. Experimental calibration of aluminum partitioning between olivine and spinel as a geothermometer. Am. Mineral. 93, 1142–1147. https://doi.org/10.2138/am.2008.2758

Weit, A., Trumbull, R.B., Keiding, J.K., Geissler, W.H., Gibson, S.A., Veksler, I.V., 2017. The magmatic system beneath the Tristan da Cunha Island: Insights from thermobarometry, melting models and geophysics. Tectonophysics, Progress in understanding passive continental margins 716, 64–76. https://doi.org/10.1016/j.tecto.2016.08.010

White, R., McKenzie, D., 1989. Magmatism at rift zones: The generation of volcanic continental margins and flood basalts. J. Geophys. Res. Solid Earth 94, 7685–7729. https://doi.org/10.1029/JB094iB06p07685

White, R.S., McKenzie, D., 1995. Mantle plumes and flood basalts. J. Geophys. Res. Solid Earth 100, 17543–17585. https://doi.org/10.1029/95JB01585

Wignall, P.B., 2001. Large igneous provinces and mass extinctions. Earth-Sci. Rev. 53, 1–33. https://doi.org/10.1016/S0012-8252(00)00037-4

Wood, B.J., Virgo, D., 1989. Upper mantle oxidation state: Ferric iron contents of lherzolite spinels by 57Fe Mössbauer spectroscopy and resultant oxygen fugacities. Geochim. Cosmochim. Acta 53, 1277–1291. https://doi.org/10.1016/0016-7037(89)90062-8

Xu, R., Liu, Y., 2016. Al-in-olivine thermometry evidence for the mantle plume origin of the Emeishan large igneous province. Lithos 266–267, 362–366. https://doi.org/10.1016/j.lithos.2016.10.016

Yaxley, G.M., Green, D.H., 1998. Reactions between eclogite and peridotite: Mantle refertilisation by subduction of oceanic crust. Schweiz. Miner. Petrog. 78, 243–255.

Zhukova, I., O'Neill, H., Campbell, I.H., 2017. A subsidiary fast-diffusing substitution

mechanism of Al in forsterite investigated using diffusion experiments under controlled thermodynamic conditions. Contrib. Mineral. Petrol. 172, 53. https://doi.org/10.1007/s00410-017-1365-x

9 Figure captions

Figure 1: BSE image of an olivine crystal with abundant Cr-spinel inclusions and a rehomogenised melt inclusions (note that analyses for this study were only performed on unheated samples).

Figure 2: Simulated apparent Al_2O_3 concentrations at 15 keV in trace-element-free Fo_{90} olivine, at various distances from the edge of a 10 μm (circles) or 20 μm (triangles) diameter spherical $MgAl_2O_4$ spinel inclusion, polished through the mid-section. For simulation details, see text. Closer than 2 μm, beam convolution leads to a much higher (primary) signal that is not shown. The detection limit range of this study is shaded in orange, indicating that for a 10 – 20 μm diameter inclusion, fluorescence is below detection when olivine is measured at least 4 μm from the interface; greater distances will be needed for larger inclusions.

Figure 3: Al_2O_3 concentration in olivine (wt. %) as a function of Fo content. Red filled circles are from picrite samples; yellow filled circles are from ferropicrite samples. This plot shows the data prior to the filters of Figure 4 being applied.

Figure 4: The compositions of spinel inclusions, and their relationship to crystallisation temperature. a) Histogram showing distribution of Ti concentrations (p.f.u.) of the picrite (red) and ferropicrite (yellow) spinels. b) Histogram showing distribution of the spinel $Fe^{3+}/\Sigma Fe$ ratios. c) Crystallisation temperature (calculated using equation [1]) as a function of Ti (p.f.u in

spinel); uncertainties are 1σ and from uncertainties in Al analyses. d) Crystallisation temperature as a function of $Fe^{3+}/\Sigma Fe$. The blue solid line represents the highest content of a spinel used in the calibration dataset (Coogan et al., 2014). The red and yellow dashed lines represent our chosen limits for Ti content of the picrites and ferropicrites, respectively.

Figure 5: Histograms and probability distribution functions (PDFs) of the Al-in-olivine crystallisation temperatures of: a) all picrite olivine-spinel pairs; b) picrite pairs (Fo>90 olivines only); c) all ferropicrite pairs. Spinels with Ti contents over the limits shown in Figure 4 are excluded. The PDFs are calculated using a kernel density estimate and incorporate the individual 1σ temperature uncertainties.

Figure 6: Al-in-olivine crystallisation temperatures as a function of olivine Fo content. Red symbols are for picrite samples; yellow symbols are for ferropicrite samples. Symbol shapes indicate the sample number. Uncertainties are 1σ. The blue curve shows a model fractional crystallisation trend for olivine in a picritic magma (see text for details): ticks are at F=0.01 intervals and the crystallising assemblage is labelled.

Figure 7: a) Histogram showing frequency of crystallisation temperatures reported from Al-in-olivine thermometry in different plume-related settings. Acronyms: NAIP, North Atlantic Igneous Province; CLIP, Caribbean Igneous Province. b) Probability distribution functions of reported Al-in-olivine temperatures grouped by setting as LIP, MORB, and Iceland. Data sources: MORB and Madagascar, Coogan et al. (2014); NAIP, Coogan et al. (2014) and Spice et al. (2016); Karoo, Heinonen et al. (2015); Emeishan, Xu and Liu (2016); CLIP, Coogan et al. (2014) and Trela et al. (2017); Iceland, Matthews et al. (2016) and Spice et al. (2016, including Tertiary Icelandic samples); Etendeka, this study (picrites and ferropicrites).

Figure 8: An example of a calculated T-P path for upwelling mantle and its melt. Thick black line, LAB, lithosphere-asthenosphere boundary; red line, thermal path; pink shaded region, uncertainty envelope; dashed lines, solid adiabat (T_P); thin black line, solidus. Closed black circle is the mean crystallisation temperature of $Fo_{>90}$ olivine and error bars are 1σ. Red line indicates the melt path: initially at depth, a solid adiabat is followed, but on reaching the solidus, the enthalpy of fusion decreases the temperature more rapidly with pressure. A kink is seen where clinopyroxene is exhausted (cpx-out) and melt productivity decreases. Melting ceases at the LAB, and a liquid adiabat is followed from here to the crystallisation pressure. The calculation is run as a forward model to find a T_P to match the $Fo_{>90}$ olivine temperature. Details in Jennings et al. (2016).

Figure 9: The modelled T_P required to match the mean crystallisation temperature of picrite $Fo_{>90}$ olivine, shown as a function of: a) lithospheric thickness; and b) melt fraction F, calculated for an emplacement (crystallisation) pressure P_{cryst} of 0.5 GPa (solid line) and 1.0 GPa (dashed line). In a) the closed red circles represent increments of F, and in b) the closed red circles represent increments of lithospheric thickness. F is a function of T_P and lithospheric thickness.

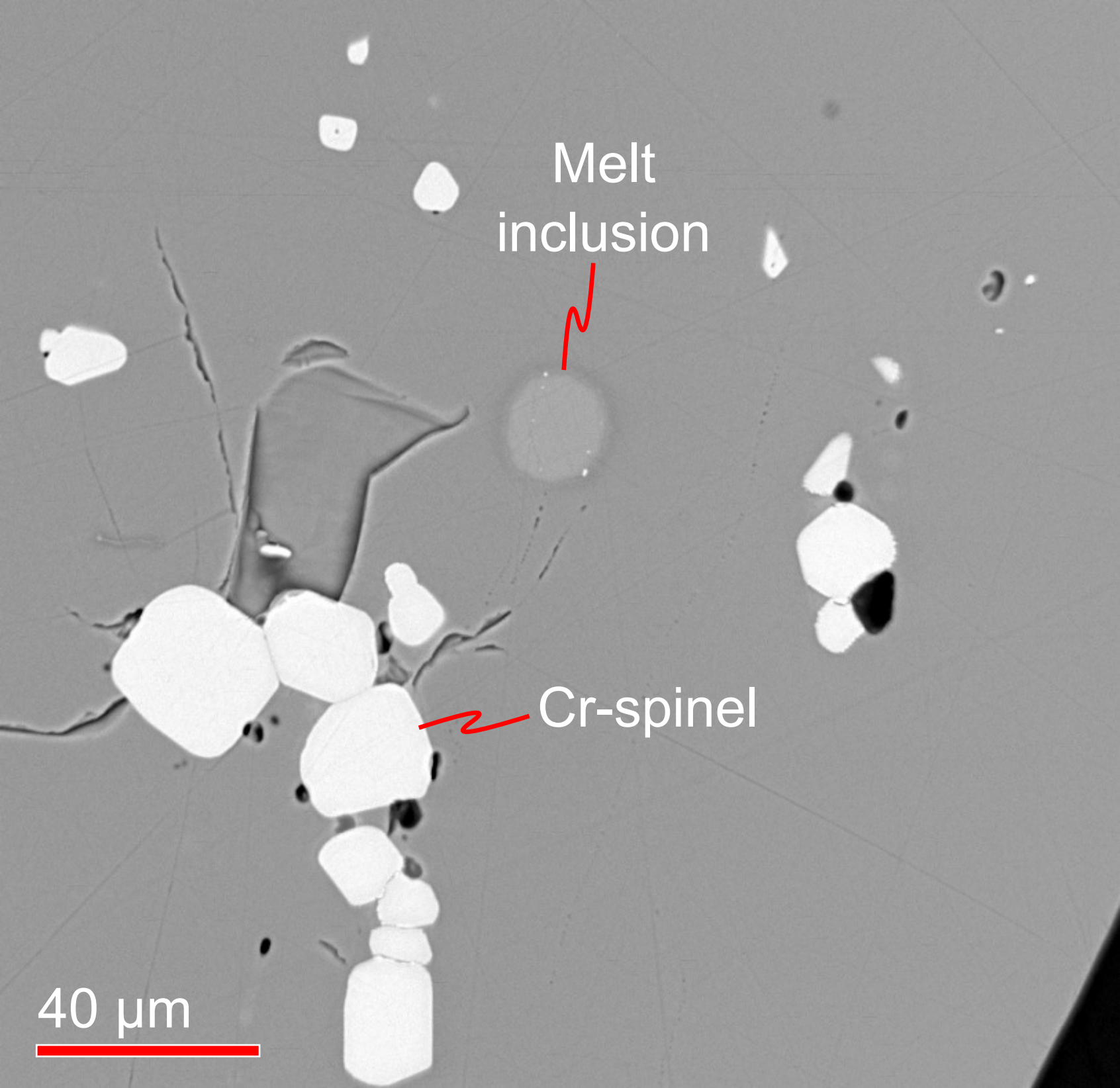
Melt
inclusion
Cr-spinel
40 µm

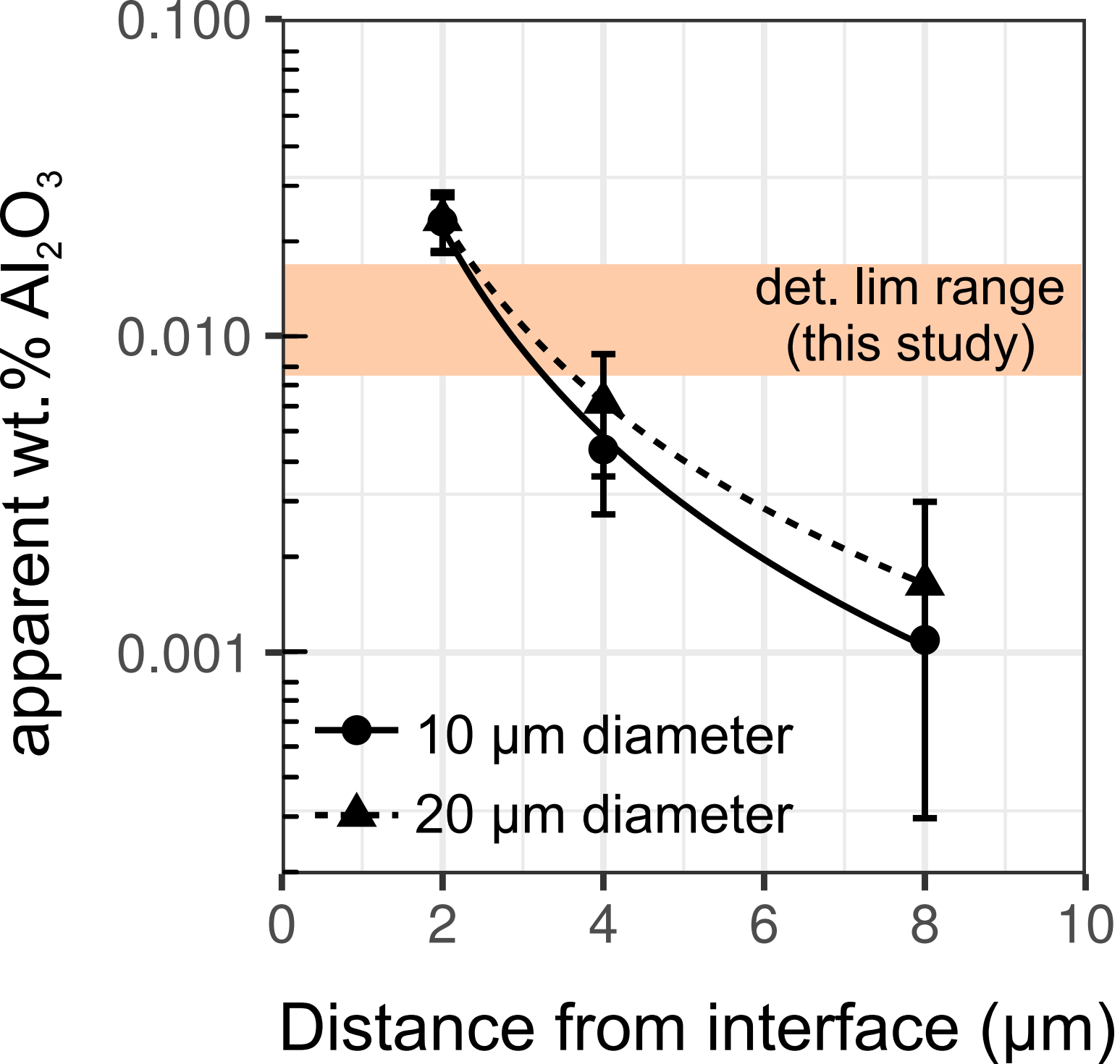
0.100
0.010
0.001
apparent wt.% Al_2O_3
det. lim range
(this study)
10 μm diameter
20 μm diameter
0
2
4
6
8
10
Distance from interface (μm)

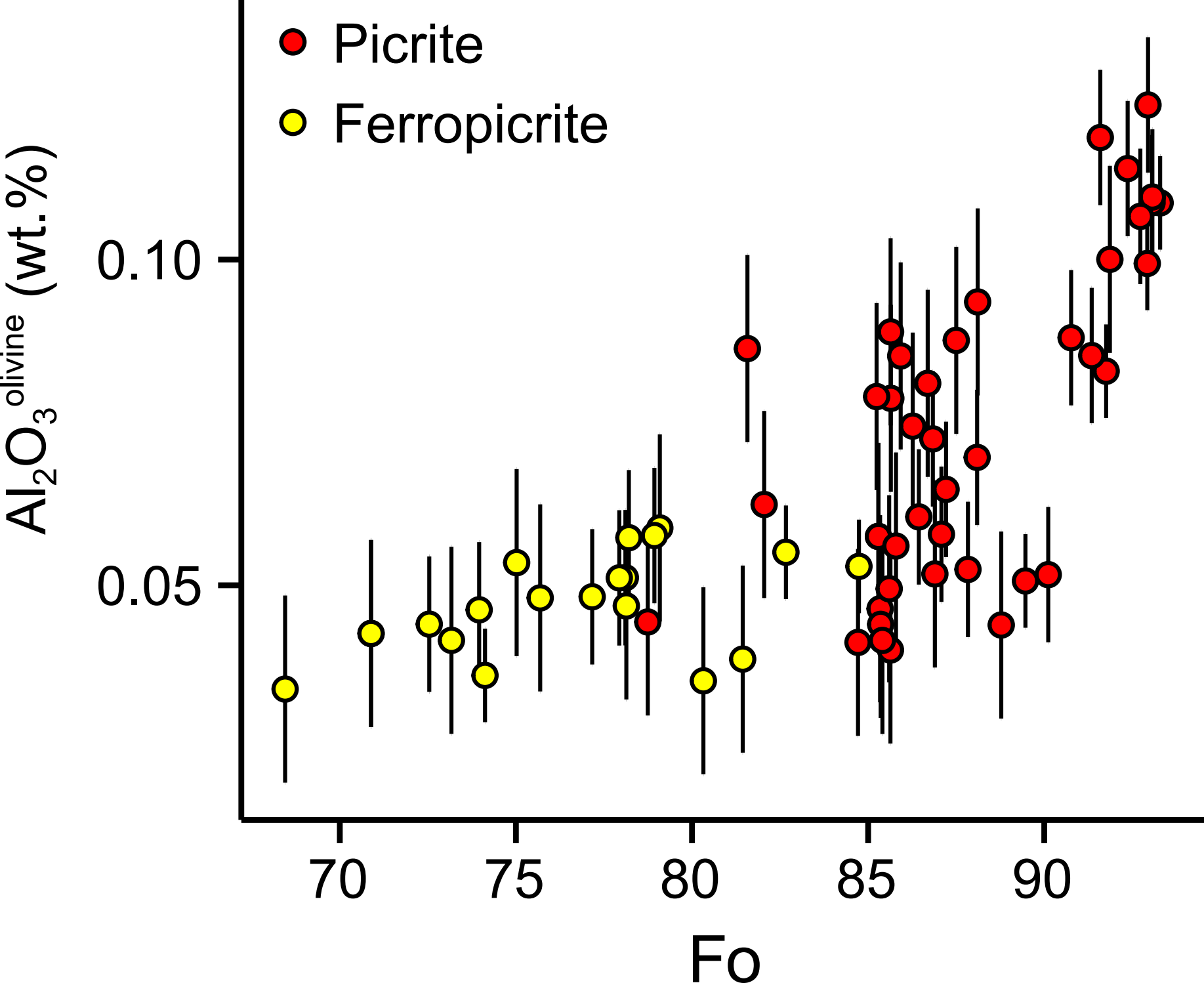
Picrite
Ferropicrite
0.10
0.05
$Al_2O_3^{olivine}$ (wt.%)
70
75
80
85
90
Fo

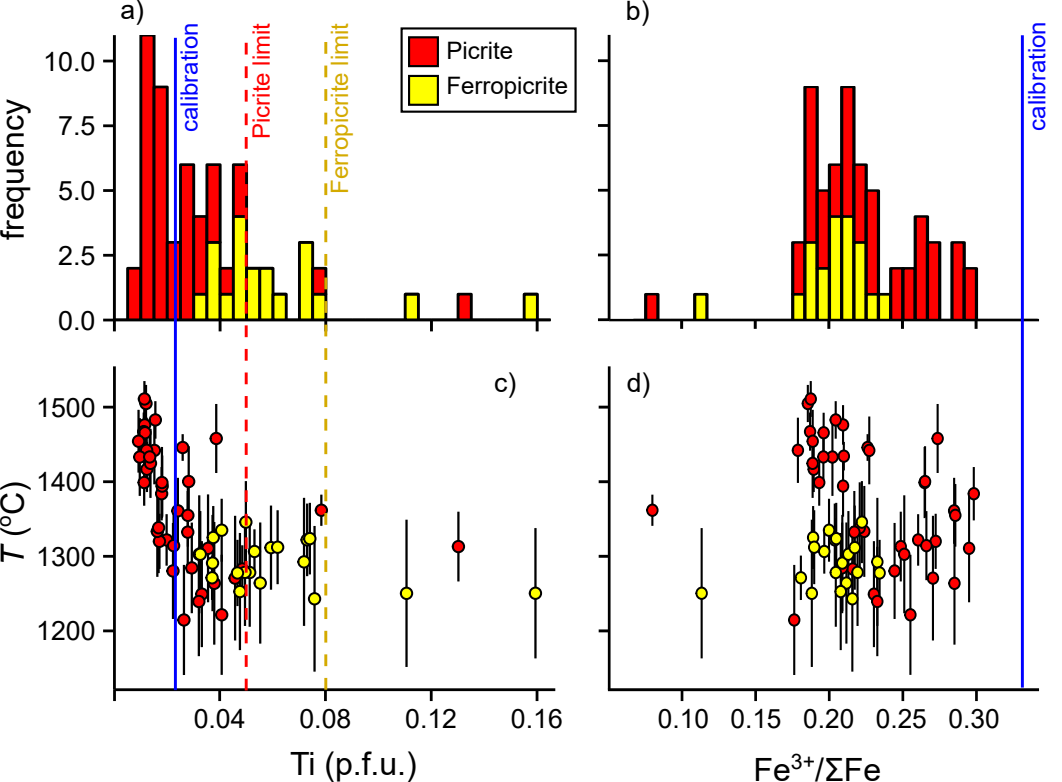
a)
b)
c)
d)
frequency
calibration
Picrite limit
Ferropicrite limit
Picrite
Ferropicrite
10.0
7.5
5.0
2.5
0.0
T (°C)
1500
1400
1300
1200
0.04
0.08
0.12
0.16
Ti (p.f.u.)
0.10
0.15
0.20
0.25
0.30
Fe3+/ΣFe

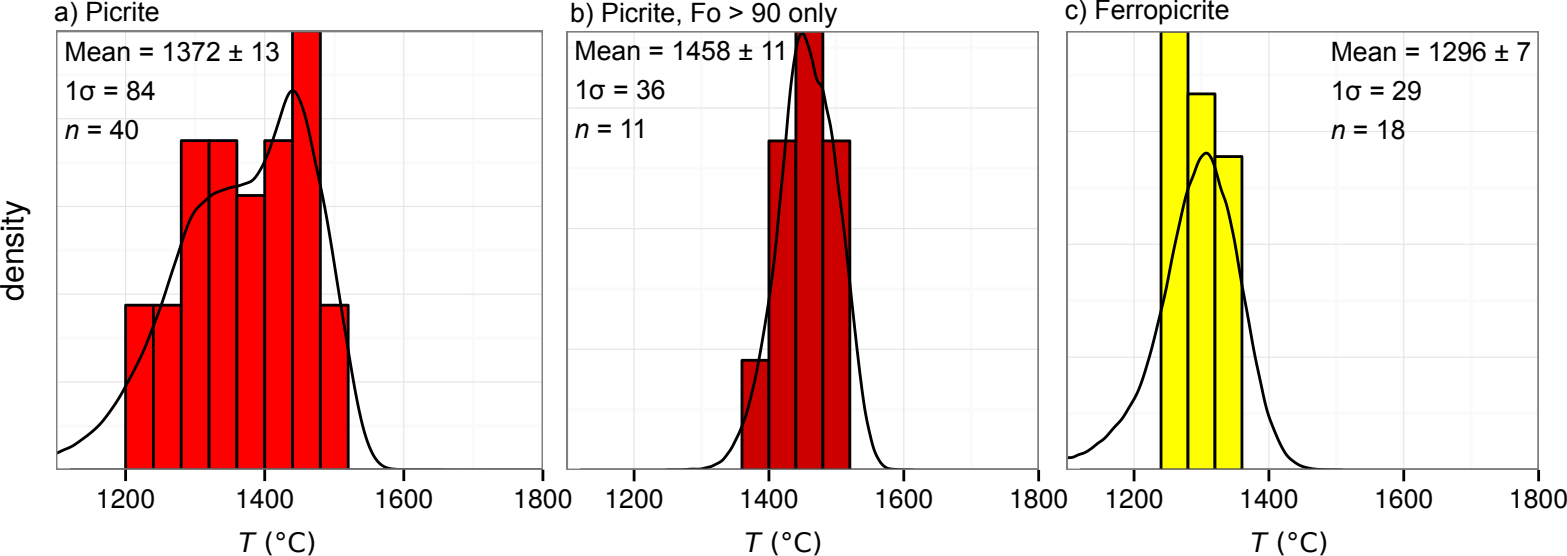
a) Picrite
Mean = 1372 ± 13
1σ = 84
n = 40
b) Picrite, Fo > 90 only
Mean = 1458 ± 11
1σ = 36
n = 11
c) Ferropicrite
Mean = 1296 ± 7
1σ = 29
n = 18
density
1200
1400
1600
1800
T (°C)

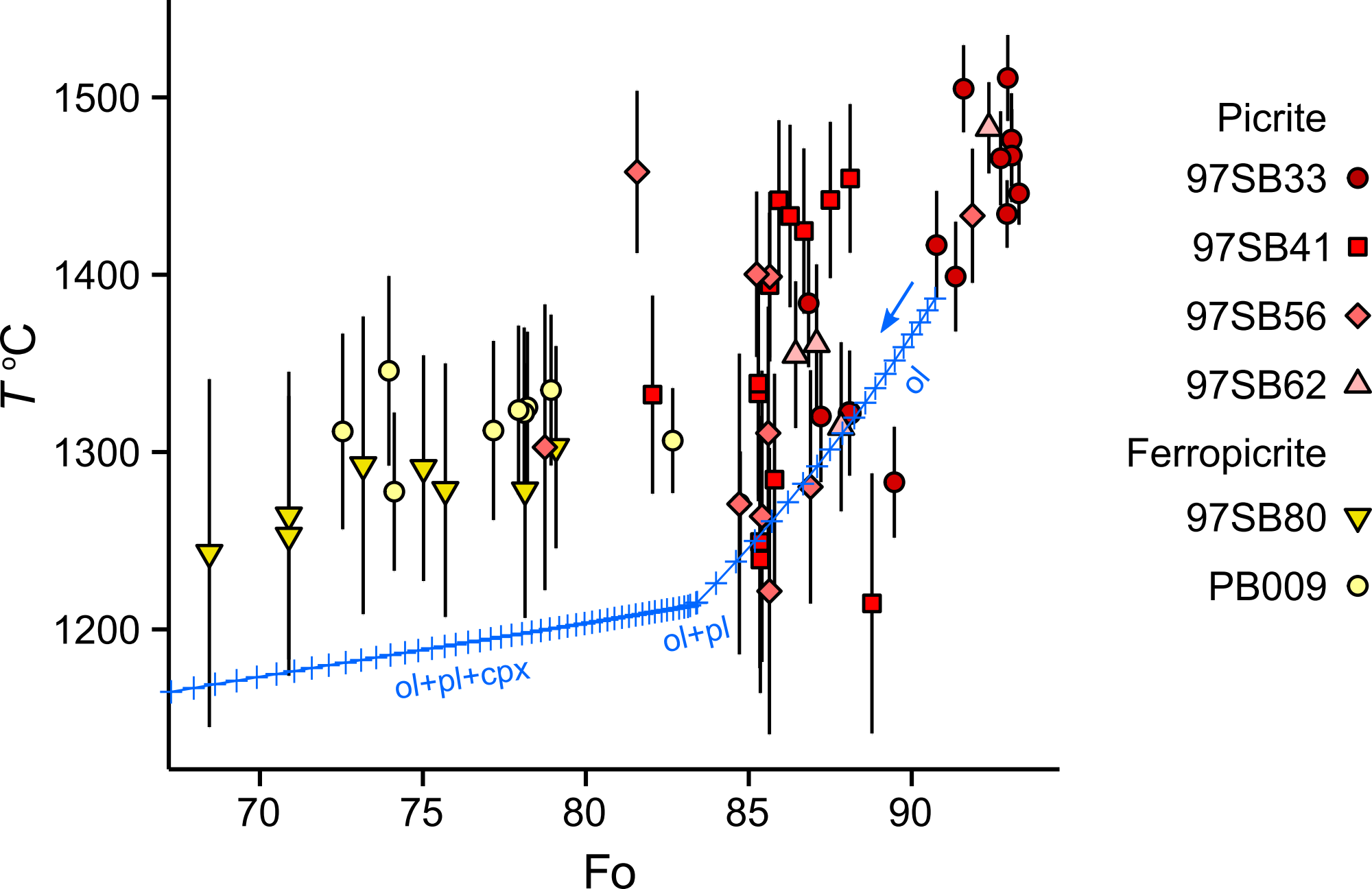
1500
1400
1300
1200
T °C
70
75
80
85
90
Fo
ol+pl+cpx
ol+pl
ol
Picrite
97SB33
97SB41
97SB56
97SB62
Ferropicrite
97SB80
PB009

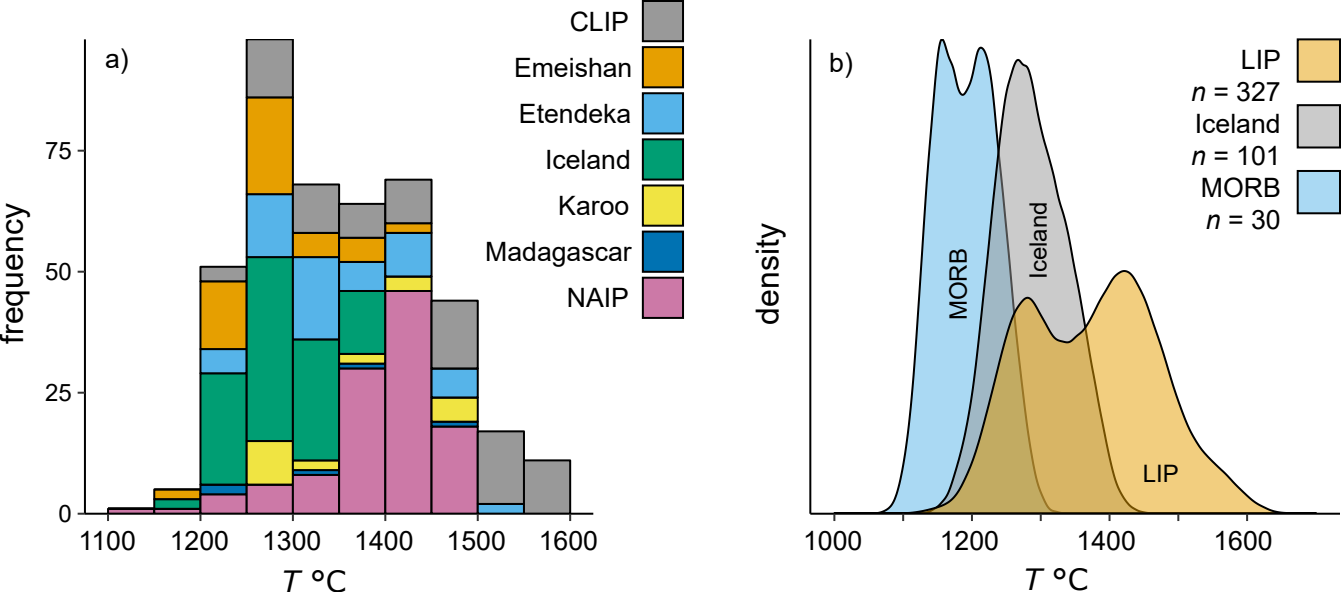
a)
frequency
0
25
50
75
1100
1200
1300
1400
1500
1600
T °C
CLIP
Emeishan
Etendeka
Iceland
Karoo
Madagascar
NAIP
b)
density
1000
1200
1400
1600
T °C
MORB
Iceland
LIP
LIP
n = 327
Iceland
n = 101
MORB
n = 30

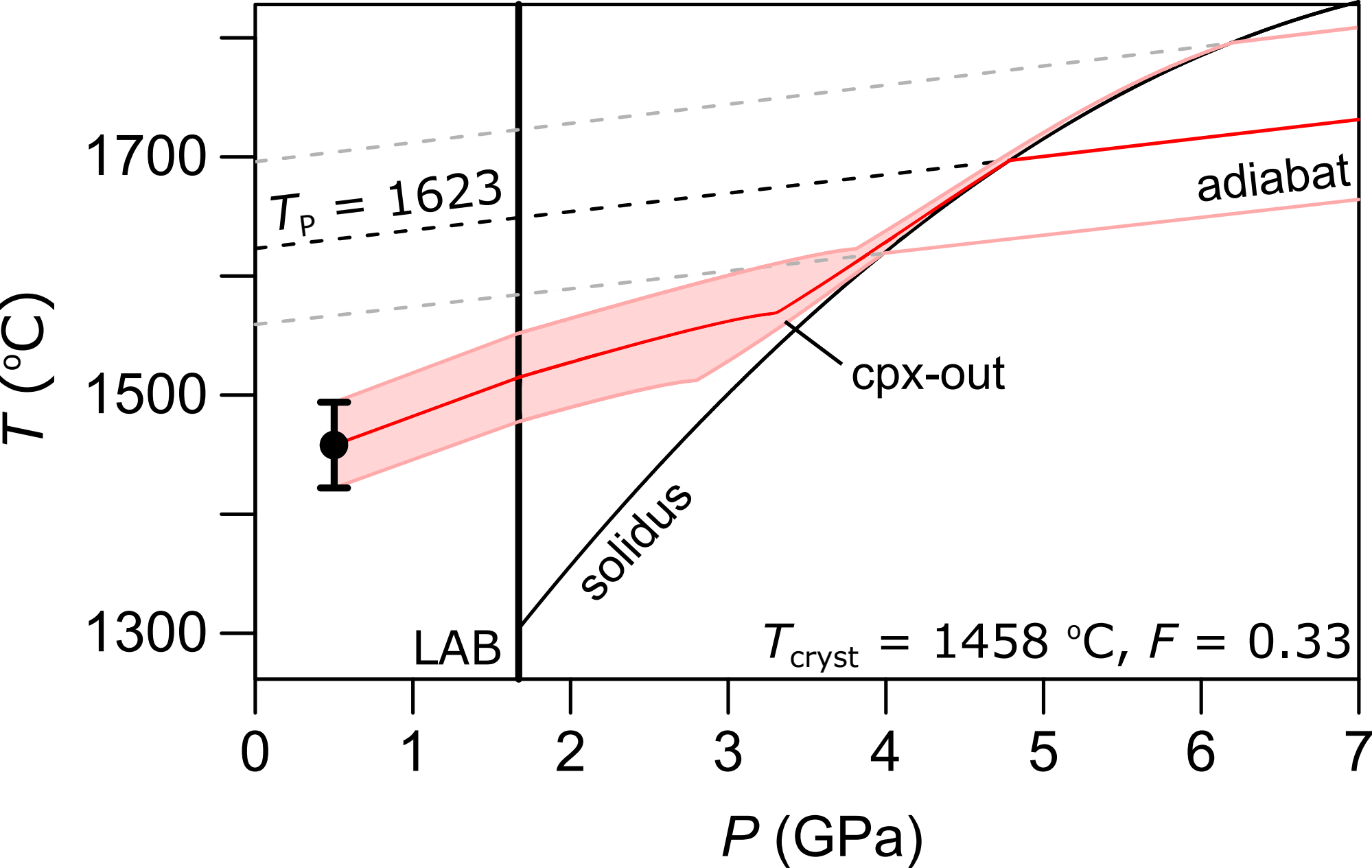
1700
1500
1300
T (°C)
T_P = 1623
adiabat
cpx-out
solidus
LAB
T_cryst = 1458 °C, F = 0.33
0
1
2
3
4
5
6
7
P (GPa)

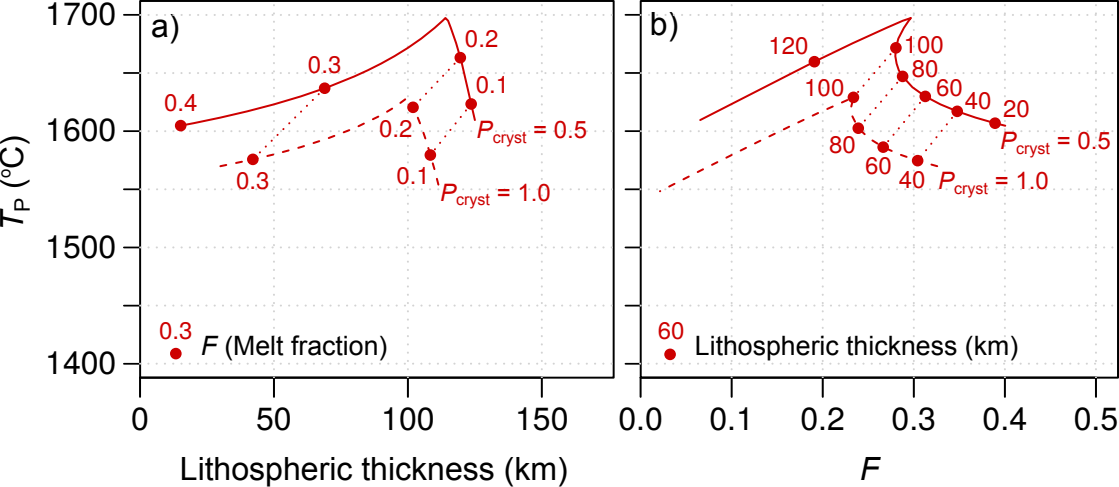
a)
b)
1700
1600
1500
1400
T_P (°C)
0.4
0.3
0.2
0.1
P_{cryst} = 0.5
P_{cryst} = 1.0
0.3
F (Melt fraction)
0
50
100
150
Lithospheric thickness (km)
120
100
80
60
40
20
P_{cryst} = 0.5
P_{cryst} = 1.0
60
Lithospheric thickness (km)
0.0
0.1
0.2
0.3
0.4
0.5
F